Backbone Dynamics of Receptor Binding and Antigenic Regions of a Pseudomonas aeruginosa Pilin Monomer †

5 AUTHORS, INCLUDING:

David Wicher Keizer
University of Melbourne
25 PUBLICATIONS **703** CITATIONS

SEE PROFILE

Randall T Irvin
University of Alberta
107 PUBLICATIONS **4,206** CITATIONS

SEE PROFILE

Brian Douglas Sykes
University of Alberta
565 PUBLICATIONS **27,432** CITATIONS

SEE PROFILE

Backbone Dynamics of Receptor Binding and Antigenic Regions of a *Pseudomonas aeruginosa* Pilin Monomer[†]

Jeong-Yong Suh,[‡] Leo Spyracopoulos,[§] David W. Keizer,[‡] Randall T. Irvin,[‡] and Brian D. Sykes*,[‡],[§]

Protein Engineering Network Centers of Excellence (PENCE), 713 Heritage Medical Research Center, University of Alberta, Edmonton, Alberta, T6G 2S2, Canada, and Department of Biochemistry, University of Alberta, Edmonton, Alberta, T6G 2H7, Canada

ABSTRACT: Pilin is the major structural protein that forms type IV pili of various pathogenic bacteria, including *Pseudomonas aeruginosa*. Pilin is involved in attachment of the bacterium to host cells during infection, in the initiation of immune response, and serves as a receptor for a variety of bacteriophage. We have used ^{15}N nuclear magnetic resonance relaxation measurements to probe the backbone dynamics of an N-terminally truncated monomeric pilin from *P. aeruginosa* strain K122-4. ^{15}N-T_1, -T_2, and {^{1}H}-^{15}N nuclear Overhauser enhancement measurements were carried out at three magnetic field strengths. The measurements were interpreted using the Lipari−Szabo model-free analysis, which reveals the amplitude of spatial restriction for backbone N−NH bond vectors with respect to nano- to picosecond time-scale motions. Regions of well-defined secondary structure exhibited consistently low-amplitude spatial fluctuations, while the terminal and loop regions showed larger amplitude motions in the subnano- to picosecond time-scale. Interestingly, the C-terminal disulfide loop region that contains the receptor binding domain was found to be relatively rigid on the pico- to nanosecond time-scale but exhibited motion in the micro- to millisecond time-scale. It is notable that this disulfide loop displays a conserved antigenic epitope and mediates binding to the asialo-GM$_1$ cell surface receptor. The present study suggests that a rigid backbone scaffold mediates attachment to the host cell receptor, and also maintains the conformation of the conserved antigenic epitope for antibody recognition. In addition, slower millisecond time-scale motions are likely to be crucial for conferring a range of specificity for these interactions. Characterization of pilin dynamics will aid in developing a detailed understanding of infection, and will facilitate the design of more efficient anti-adhesin synthetic vaccines and therapeutics against pathogenic bacteria containing type IV pili.

Pseudomonas aeruginosa pilin is the structural protein of the pili produced by this organism. *P. aeruginosa* pili are type IV pili, that constitute long linear fibers forming a filamentous appendage extending from the poles of the cell consisting of a helical array of the structural protein (*1*). Type IV pili are critical virulence factors in bacterial pathogenesis (*2, 3*). They are bacterial adhesins (*4*), function as phage receptors (*5, 6*), and are responsible for a type of cellular motion known as twitching motility (*7, 8*). Type IV pili are widely distributed among pathogenic bacteria, being found in organisms such as *P. aeruginosa*, *Neisseria gonorrhoeae*, *N. meningitidis*, *Vibrio cholorea*, *Moraxella bovis*, *M. catarrahlis*, and *Escherichia coli* (*9, 10*). The pilin protein is of considerable interest due to its critical role in pathogenesis and the variety of molecular interactions that this protein is involved in.

The first crystal structure of a pilin was determined from *N. gonorrhoeae* strain MS11 (*11*). Recently, the structure of a second pilin from *P. aeruginosa* strain K (PAK)[1] has been determined by X-ray crystallography (*12*). Additionally, the solution structure of pilin from *P. aeruginosa* strain K122-4 has been determined from NMR spectroscopy (Keizer et al., unpublished). The structural studies on *P. aeruginosa* pilins utilize an N-terminally truncated pilin to inhibit oligomerization. The removal of the first 28 residues does not alter the structure of the intact protein (Keizer et al., unpublished). Pilin from strain K122-4 is a 150-residue protein comprised of a long N-terminal α-helix, a 4-stranded antiparallel β-sheet, and 2 disulfide bonds. The C-terminal disulfide loop region is hypervariable, and the central region is semi-conserved (*13*). The receptor binding domains of pilins from various strains share a common C-terminal motif that includes a disulfide bridge (*12*). The C-terminal disulfide loop region from the binding domain of pilin plays an important role in adhesion of bacteria to host cells, and in triggering the immune response of the infected host cells (*14, 15*). The conformation of this loop region forms a conserved two β-turn motif, as determined from the solution structure of synthetic peptide fragments (*16, 17*).

* Address correspondence to this author at PENCE, 713 Heritage Medical Research Centre, Edmonton, T6G 2S2, Alberta, Canada. Fax: (780) 492 1473, Phone: (780) 492 6540, Email: brian.sykes@ualberta.ca.
[‡] PENCE, University of Alberta.
[§] Department of Biochemistry, University of Alberta.

[1] Abbreviations: HSQC, heteronuclear single-quantum coherence; NOE, nuclear Overhauser enhancement; PAK, *Pseudomonas aeruginosa* strain K; rmsd, root-mean-square deviation.

Protein function commonly involves the interaction of a protein with different ligands. Studies aimed at elucidating the structure of interfaces of protein−ligand complexes contribute to our basic understanding of protein function. Additionally, the flexibility of the protein and ligand, and the flexibility of the interface in the bound state determine in part the interaction affinity. Studies of protein dynamics are therefore important in order to gain an understanding of the molecular processes underlying recognition, and their relationship to protein function. The unison of three-dimensional structure determination and measurements of time-dependent conformational fluctuations of proteins using NMR methodologies have provided detailed insight into biological function (*18, 19*). Concomitant with the advent of sophisticated multinuclear, multidimensional magnetic resonance techniques, and the availability of highly isotope-enriched proteins, detailed atomic maps of the dynamic behavior of proteins have been made possible using NMR relaxation measurements (*20, 21*). Measurement of NMR relaxation of backbone amide ^{15}N and backbone ^{13}C$_\alpha$ nuclei provides valuable information regarding backbone motions, whereas relaxation of ^{13}C and ^{2}H nuclei affords insight into side chain mobility. Moreover, thermodynamic properties, such as conformational entropy and heat capacity, can be determined in a semiquantitative fashion from relaxation parameters, and are especially interesting due to the relationship to function (*22, 23*). In this study, the backbone dynamics of K122-4 pilin were investigated using ^{15}N NMR relaxation and the results discussed with respect to functional implications.

EXPERIMENTAL PROCEDURES

Sample Preparation. The expression and purification of ^{15}N-labeled K122-4 pilin$^{(29−150)}$ will be published elsewhere. Of 150 residues, 28 were removed from the N-terminus to prevent oligomerization. Seven residues were added to the N-terminus to allow for the cloning and expression of periplasmically localized protein. Thus, the K122-4 pilin$^{(29−150)}$ used in this study totaled 129 residues. The amino acid sequence and ^{15}N-T_1, -T_2, and {^{1}H}-^{15}N NOE values are included as supporting information (see Supporting Information). The sample was prepared for NMR spectroscopy by dissolving lyophilized protein in 20 mM deuterated sodium acetate buffer (90% H$_2$O/10% D$_2$O) containing 1 mM sodium azide, and 1 mM DSS (2,2-dimethylsilapentane-5-sulfonic acid). The final protein concentration was 0.5 mM, and the pH was adjusted to 5.1 with microliter aliquots of 1 M HCl.

NMR Spectroscopy. NMR spectra were acquired using Varian Unity INOVA 500 MHz and Unity 600 MHz spectrometers equipped with 5 mm triple resonance probes and z-axis pulsed field gradients, and a Varian Unity 300 MHz spectrometer with a 5 mm inverse broadband probe. ^{15}N-T_1, -T_2, and {^{1}H}-^{15}N NOE experiments were conducted at 30 °C using sensitivity-enhanced gradient pulse sequences developed by Farrow et al. (*24*) and at 500 and 600 MHz. Sensitivity-enhanced, nongradient pulse sequences written in-house (*25*) were employed at 300 MHz. Relaxation measurements at different temperatures were carried out at 500 MHz with temperatures ranging from 5 to 35 °C in 10 °C steps. For measurement of ^{15}N-T_1 relaxation times, delays of 10, 50, 100, 150, 200, 300, 400, and 600 ms were used at 300 MHz, and delays of 11.1, 55.5, 122.1, 199.8, 277.5,

388.5, 499.5, 666, 888, and 1110 ms were used at 500 and 600 MHz. For measurement of ^{15}N-T_2 relaxation times, delays of 15.49, 30.98, 46.46, 61.95, 77.44, 92.93, 108.42, and 123.90 ms were employed at 300 MHz, and delays of 16.61, 33.22, 49.82, 66.43, 83.04, 99.65, 116.25, 132.86, 149.47, and 166.08 ms were used at 500 MHz. Additionally, delays of 16.54, 33.09, 49.63, 66.18, 82.72, 99.26, 115.81, 132.35, 148.90, and 165.44 ms at 600 MHz were used for measurement of ^{15}N-T_2 relaxation times. {^{1}H}-^{15}N steady-state NOEs were measured from two HSQC spectra acquired with and without proton saturation prior to the first ^{15}N excitation pulse. Proton saturation was obtained using a train of 120° proton pulses with 5 ms pulse intervals for a total 3.5 s of saturation at 300, 500, and 600 MHz. To obtain equilibrium, a 2 s delay between repetitions of the pulse sequence for ^{15}N-T_1 measurements was employed at 300 MHz, and 1.2 s at 500 and 600 MHz. Delays for obtaining equilibrium during the measurement of ^{15}N-T_2 were 2.5 s at 300 and 600 MHz, and 3 s at 500 MHz. For {^{1}H}-^{15}N NOE measurements, delays of 7 s (300 MHz) and 5 s (500 and 600 MHz) were used between repetitions of the pulse sequence. The spectral widths for ^{1}H and ^{15}N, respectively, were 4000 and 1064 Hz at 300 MHz, 6300 and 1775 Hz at 500 MHz, and 7500 and 1800 Hz for 600 MHz. The number of real data points acquired for ^{1}H and ^{15}N, respectively, were 320 and 48 points (300 MHz), 403 and 96 points (500 MHz), and 467 and 96 points (600 MHz). A total of 16 or 32 transients were collected for ^{15}N-T_1 and -T_2, and a total of 32 or 72 transients for {^{1}H}-^{15}N NOE were collected at 500 and 600 MHz, respectively. At 300 MHz, 240 transients were accumulated for ^{15}N-T_1 and -T_2 measurements, and 256 transients for measurement of {^{1}H}-^{15}N NOE.

NMR Data Processing. All NMR data were processed with the NMRPipe software (*26*). Enhanced sensitivity data were processed using the ranceY.M macro. Residual solvent suppression procedures in the time domain were not necessary. The F_1 dimension was extended by 48 complex points (500 and 600 MHz) or 24 complex points (300 MHz) using linear prediction before zero filling. The F_2 (^{1}H) dimension was multiplied by a 60°-shifted sine-bell function, and the F_1 (^{15}N) dimension was multiplied by a 75°-shifted squared sine-bell function before Fourier transformation. The F_1 and F_2 dimensions were baseline corrected by polynomial subtraction in the frequency domain.

Chemical shift assignment for K122-4 pilin has been described previously (BMRB entry 4918; *27*). Peak picking of two-dimensional {^{1}H-^{15}N}-HSQC spectra was performed using the NMRView program (*28*). Peak intensity values for ^{15}N-T_1 and -T_2 measurements were fit to single-exponential, two-parameter decays using the xcrvfit program (software available at the following address: http://www.pence.ca/ftp). Error in the ^{15}N-T_1 and -T_2 measurements was obtained from the nonlinear least-squares fits of the peak intensities to two-parameter exponential decays. Error in the {^{1}H}-^{15}N NOE measurements was calculated from baseplane noise values in two-dimensional spectra acquired with and without proton saturation.

Analysis of ^{15}N-Relaxation Data. Backbone amide ^{15}N-T_1, -T_2, and {^{1}H}-^{15}N NOE relaxation parameters are governed principally by the dipolar interaction between the ^{15}N nucleus and its attached proton, and by the chemical shift anisotropy of the ^{15}N nucleus (*29*). Theoretical expres-

sions for ^{15}N-T_1, -T_2, and {^{1}H}-^{15}N steady-state NOE relaxation parameters are given by linear combinations of a spectral density function at the Larmor frequencies of ^{15}N and ^{1}H$_N$ nuclei:

$$\frac{1}{T_1} = D[J(\omega_H - \omega_N) + 3J(\omega_N) + 6J(\omega_H + \omega_N)] +$$

$$C[J(\omega_N)] \quad (1)$$

$$\frac{1}{T_2} = \frac{D}{2}[4J(0) + J(\omega_H - \omega_N) + 3J(\omega_N) +$$

$$6J(\omega_H + \omega_N) + 6J(\omega_H)] + C\left[\frac{2}{3}J(0) + \frac{1}{2}J(\omega_N)\right] \quad (2)$$

$$\text{NOE} = 1 + \frac{\gamma_H}{\gamma_N}\left[\frac{D[6J(\omega_H + \omega_N) - J(\omega_H - \omega_N)]}{1/T_1}\right] \quad (3)$$

where $D = (\mu_0/4\pi)^2(\gamma_H^2\gamma_N^2\hbar^2/4r_{NH}^6)$ and $C = \Delta^2\omega_N^2/3$, μ_0 is the permeability constant of free space ($4\pi \times 10^{-7}$ kg m s^{-2} A^{-2}), γ_H is the proton magnetogyric ratio (2.68×10^8 rad s^{-1} T^{-1}), γ_N is the magnetogyric ratio of ^{15}N (-2.71×10^7 rad s^{-1} T^{-1}), r_{NH} is the proton−nitrogen internuclear separation (102 pm), Δ is the difference between the parallel and perpendicular components of the ^{15}N chemical shift tensor (-160 ppm), $\hbar$ is Planck's constant divided by 2π (1.05×10^{-34} J s), and ω_N is the Larmor frequency of ^{15}N. Typically, the spectral density is a Lorentzian function with respect to frequency. In the Lipari−Szabo analysis, the spectral density is formulated in terms of an order parameter (S^2) that indicates the degree of spatial restriction for a backbone amide N−NH bond vector, with an associated internal correlation time, and with the assumption of a single, global molecular rotational correlation time (*30, 31*):

$$J(\omega) = \frac{2}{5}\left[\frac{S^2\tau_m}{(1 + \omega^2\tau_m^2)} + \frac{(1 - S^2)\tau}{(1 + \omega^2\tau^2)}\right] \quad (4)$$

where $\tau^{-1} = \tau_m^{-1} + \tau_e^{-1}$, S^2 is the generalized order parameter, τ_m is the correlation time for overall molecular tumbling, and τ_e is the correlation time for internal motion. For each residue, relaxation data were fit to a spectral density model which included overall molecular tumbling of the protein, with one or two types of internal motions with various time-scales. The basic motional model is typically separated into five specific models. These included model 1 with S^2 describing the amplitude of spatial restriction for a backbone amide N−NH vector which can vary from 0 (no spatial restriction) to 1 (complete spatial restriction), and τ_m. Model 2 is with S^2, τ_m, and a correlation time for picosecond time-scale internal motions (τ_e). Model 1 assumes that $\tau_e \rightarrow$ 0 and does not contribute to relaxation, whereas model 2 assumes that internal motions are within the $10^{-10}-10^{-12}$ s time-scale ($0 < \tau_e < \tau_m$) and contribute to relaxation. Model 3 is model 1 modified to include a parameter describing the contribution of microsecond to millisecond time-scale internal motions to $1/T_2$ (R_{ex}, in s^{-1}). Model 4 is a modification of model 2 to include the parameter R_{ex}. Model 5 accounts for internal motions occurring on two time-scales. This model consists of an order parameter for fast picosecond internal motions (S_f^2), an order parameter for nanosecond time-scale internal motions faster than τ_m but slower than τ_e (S_s^2), a

correlation time for picosecond internal motions, assumed not to contribute to relaxation ($\tau_e \rightarrow 0$), and a correlation time for nanosecond time-scale internal motions (τ_s):

$$J(\omega) = \frac{2}{5}\left[\frac{S^2\tau_m}{(1 + \omega^2\tau_m^2)} + \frac{(S_f^2 - S^2)\tau_s'}{(1 + \omega^2\tau_s'^2)}\right] \quad (5)$$

where $S^2 = S_f^2 S_s^2$ and $\tau_s' = \tau_s\tau_m/(\tau_s + \tau_m)$. For each residue, parameters for each model of the spectral density function were adjusted to minimize the objective function given in eq 6:

$$\chi^2 = \frac{(T_{1,c} - T_{1,e})^2}{\sigma_{T_1}^2} + \frac{(T_{2,c} - T_{2,e})^2}{\sigma_{T_2}^2} + \frac{(\text{NOE}_c - \text{NOE}_e)^2}{\sigma_{\text{NOE}}^2}$$

$$(6)$$

where the subscripts c and e indicate calculated and experimental values, respectively, and σ is the error of the individual relaxation parameters. In addition, we have analyzed the ^{15}N relaxation data under the assumption of axially symmetric rotational diffusion. Theoretical expressions for the spectral density in this case maybe found in reference *32*.

RESULTS

^{15}N-T_1, -T_2, and NOE Data. The K122-4 pilin$^{(29-150)}$ used in this study consists of 129 residues as described under Experimental Procedures. The first seven residues, not part of the native protein sequence, were numbered 22−28. Sequence numbering is based on the intact 150-residue protein. Backbone amide protons were unambiguously assigned for 115 out of the 125 non-proline residues. Resonances for the remaining amide protons either were not observed or were degenerate (*27*). Due to overlap in {^{1}H-^{15}N}-HSQC spectra, 100 residues at 300 MHz, 110 residues at 500 MHz, and 112 residues at 600 MHz were used for the relaxation analysis. Typical examples of the decay of cross-peak intensities as a function of ^{15}N-T_1 and -T_2 and associated fits to two-parameter exponential decays at three fields are shown in Figure 1. Values of ^{15}N-T_1, -T_2, and {^{1}H}-^{15}N NOE as a function of residue number are shown in Figure 2. The profiles of ^{15}N-T_1, -T_2, and {^{1}H}-^{15}N NOE values for the three magnetic field strengths exhibit similar patterns as a function of residue number (Figure 2). For proteins in the slow tumbling limit with $\tau_m \geq 5$ ns, ^{15}N-T_1 values are largely determined by rates of motion that occur at the Larmor frequency of ^{15}N and therefore show a characteristic magnetic field strength dependence (Figure 2). The average T_1^{300} was 298 ± 40 ms with an average error of 8 ms, T_1^{500} was 526 ± 40 ms with an average error of 7 ms, and T_1^{600} was 638 ± 43 ms with an average error of 14 ms for all residues. T_2 values in the slow tumbling limit are determined in large part by the value of the spectral density at zero frequency, $J(0)$, and thus are expected to be similar at different magnetic field strengths, in the absence of chemical or conformational exchange contributions to T_2. The average T_2^{300} was 108 ± 31 ms with an average error of 5 ms, T_2^{500} was 116 ± 32 ms with an average error of 1 ms, and T_2^{600} was 111 ± 31 ms with an average error of 1 ms. The {^{1}H}-^{15}N NOE values are particularly sensitive to fast internal motions within the

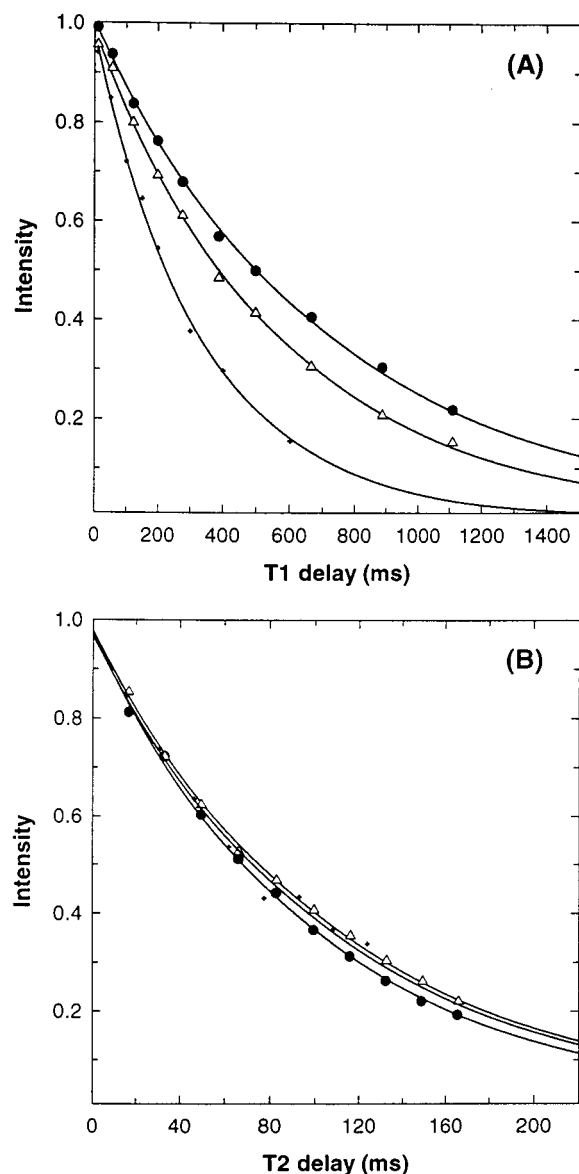FIGURE 1: Examples of (A) ^{15}N-T_1 and (B) ^{15}N-T_2 decay curves for Ala128 at 300 (+), 500 ($\triangle$), and 600 MHz ($\bullet$). Each curve was fit to a two-parameter single-exponential decay. The ^{15}N-T_1 values were 298 ± 40, 526 ± 40, and 638 ± 43 ms, and the ^{15}N-T_2 values were 108 ± 31, 116 ± 32, and 111 ± 31 ms at 300, 500, and 600 MHz, respectively.

10^{-10}–10^{-12} s time-scale ($0 < \tau_e < \tau_m$), and a similar pattern is observed at the three magnetic field strengths as a function of residue. The average NOE^{300} was 0.72 ± 0.09 with an average error of 0.09, NOE^{500} was 0.72 ± 0.05 with an average error of 0.03, and NOE^{600} was 0.75 ± 0.04 with an average error of 0.01 for all residues used in this study. The average errors were 2.6%, 1.3%, and 2.3% for T_1, and 4.7%, 1.2%, and 0.8% for T_2 at 300, 500, and 600 MHz, respectively.

Rotational Diffusion Anisotropy and Overall Correlation Time. To calculate a global τ_m, residues for which internal motions in the 10^{-10}–10^{-12} s time-scale are faster than τ_m and lengthen T_1 values must be eliminated prior to the calculation. This is accomplished by using NOE values above a certain threshold, as the NOE is sensitive to the internal dynamics on the pico- to nanosecond time-scale. An NOE value of 0.6 was used as a threshold at the three magnetic

field strengths. A total of 77 out of 100 residues from the 300 MHz data set, 95 out of 110 residues from the 500 MHz data set, and 97 out of 112 residues from the 600 MHz data set were selected by the NOE criteria for use in the global τ_m calculation. Residues excluded from the global τ_m calculation using NOE criteria are 24–25, 53, 57, 62–67, 72, 77, 83, 87, 115, 120–125, 136, and 144–146 for 300 MHz data, and residues 24–25, 63–66, 120–125, and 144–146 for 500 and 600 MHz data. Residues removed from 500 and 600 MHz data are found in loop regions between regions of well-defined secondary structure. The larger number of residues removed from 300 MHz data is mainly due to larger errors associated with NOE values at 300 MHz. Ratios of the relaxation parameters between different magnetic field strengths were obtained for the residues selected by NOE criteria. For T_1 ratios, values of T_1^{600}/T_1^{500}, T_1^{500}/T_1^{300}, and T_1^{600}/T_1^{300} are 1.23 ± 0.05, 1.83 ± 0.10, and 2.25 ± 0.15, respectively. For T_2 ratios, values of T_2^{600}/T_2^{500}, T_2^{500}/T_2^{300}, and T_2^{600}/T_2^{300} are 0.97 ± 0.06, 1.08 ± 0.09, and 1.04 ± 0.11. For NOE relaxation parameters, NOE^{600}/NOE^{500}, NOE^{500}/NOE^{300}, and NOE^{600}/NOE^{300} were 1.05 ± 0.07, 1.02 ± 0.13, and 1.07 ± 0.13, respectively. These ratios are in good agreement with theoretical values of T_1^{600}/T_1^{500}, T_1^{500}/T_1^{300}, and T_1^{600}/T_1^{300} ratios of 1.26, 1.92, and 2.41, respectively, T_2^{600}/T_2^{500}, T_2^{500}/T_2^{300}, and T_2^{600}/T_2^{300} ratios of 0.96, 0.96, and 1.00, respectively, and NOE^{600}/NOE^{500}, NOE^{500}/NOE^{300}, and NOE^{600}/NOE^{300} ratios of 0.97, 0.99, and 1.00, respectively. Theoretical ratios were calculated using eqs 1–4 with $S^2 = 0.85$, $\tau_e = 100$ ps, and $\tau_m = 7.4$ ns.

Residues for which T_1/T_2 ratios are not affected by fast picosecond time-scale motions, as determined by NOE criteria, were used to estimate the global τ_m (24). In addition, residues with T_1/T_2 ratios above or below one standard deviation of the mean for all residues were removed. The relaxation parameters for the three magnetic field strengths were treated separately. The average T_1/T_2 ratios of the selected residues were 2.92 ± 0.34, 4.91 ± 0.77, and 6.25 ± 1.12 at 300, 500, and 600 MHz, respectively. A total of 52 residues were used to calculate τ_m at 300 MHz, 85 residues at 500 MHz, and 91 residues at 600 MHz. The τ_m was calculated on a per residue basis using spectral density model 2 (eq 4) for isotropic rotational diffusion, and the results were averaged to give a global τ_m (32). A global τ_m of 8.6 ns was obtained at 300 MHz, 7.5 ns at 500 MHz, and 7.3 ns at 600 MHz. The longer τ_m determined at 300 MHz, compared to the values determined from 500 and 600 MHz data, is due to systematically larger than expected T_1 values at 300 MHz. However, S^2 values determined from 300 MHz relaxation data show good agreement with those determined from 500 and 600 MHz data (see below).

The normalized lengths of the principal axes of the inertia tensor for K122-4 pilin$^{(29-150)}$ were calculated from 10 structures determined from solution NMR spectroscopy (PDB entry 1HPW). The ratio of the normalized lengths was 1.00: 0.69:0.55. Thus, anisotropy in the rotational tumbling of K122-4 pilin$^{(29-150)}$ is expected. The rotational diffusion anisotropy was examined after selecting residues not affected by large-amplitude fast picosecond and slower millisecond time-scale motions, as described by Tjandra et al. (33). The relaxation parameters were analyzed with respect to isotropic, axially symmetric, and fully asymmetric rotational tumbling models using a grid search to find the minimum in the
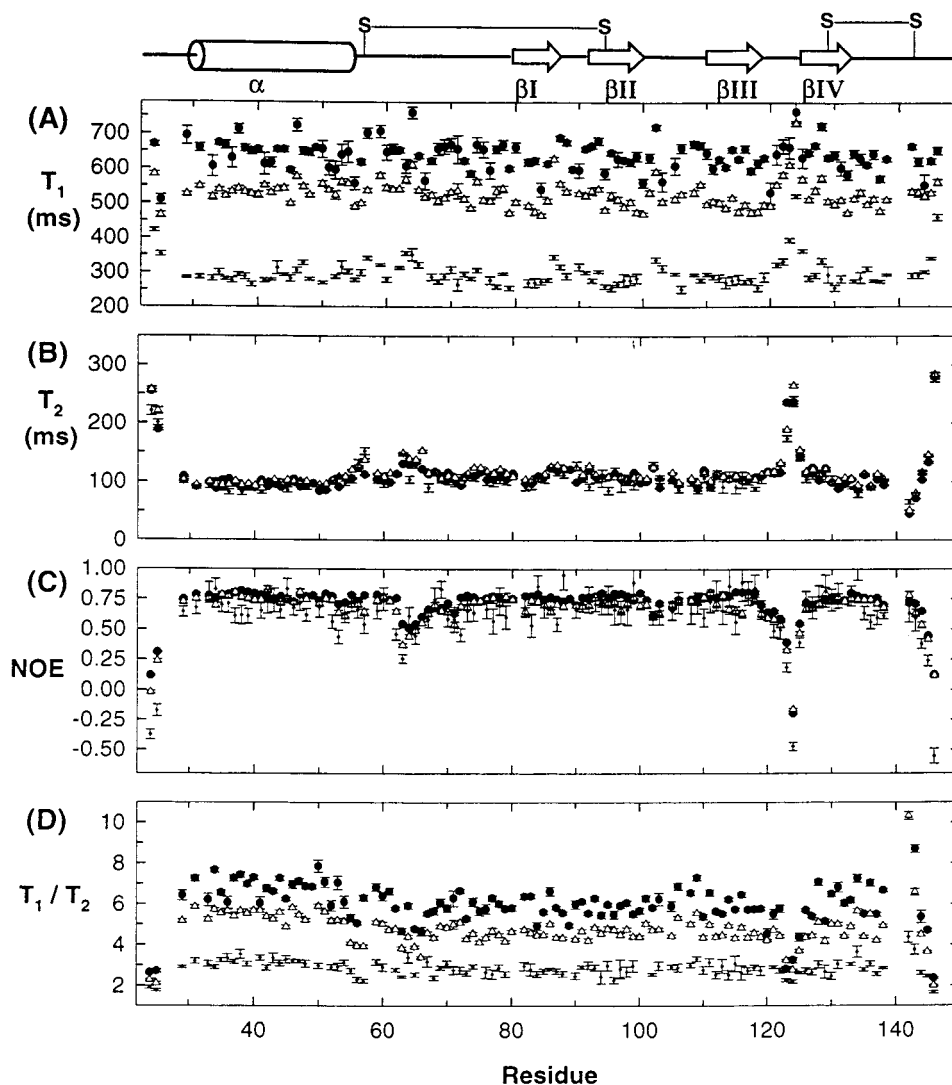
FIGURE 2: Plots of (A) ^{15}N-T_1, (B) ^{15}N-T_2, (C) $\{^1H\}$-^{15}N NOE, and (D) T_1/T_2 ratios with individual error bars at 300 (+), 500 ($\triangle$), and 600 MHz ($\bullet$). Average T_1/T_2 ratios calculated for residues with negligible internal motions (NOE > 0.6) were 2.92 $\pm$ 0.34 for T_1^{300}/T_2^{300} (+), 4.91 $\pm$ 0.77 for T_1^{500}/T_2^{500} ($\triangle$), and 6.25 $\pm$ 1.12 for T_1^{600}/T_2^{600} ($\bullet$). The T_1/T_2 ratio of Cys142 at 600 MHz is 14.7 and off the scale of the plot in panel (D). A schematic diagram of secondary structure and locations of the disulfide bonds is drawn above the panel with a cylinder depicting the α-helix and arrows depicting the β-strands. The residues in structured regions are as follows: α-helix (31−54), βI (79−87), βII (91−100), βIII (110−119), βIV (126−133). The cysteine residues in disulfide bonds are Cys57−Cys93 and Cys129−Cys142.

squared difference between measured and calculated T_1/T_2 ratios using an in-house written program (*34*). Only T_1/T_2 ratios for residues in well-defined secondary structure were considered for the anisotropic rotational tumbling analysis. The rotational tumbling of K122-4 pilin$^{(29-150)}$ is best characterized using the axially symmetric model with $D_{||}$/$D_{\perp} \cong 1.3$ at all three magnetic field strengths (Table 1). A statistical *F*-test in Table 1 validated the inclusion of additional parameters in the axially symmetric rotational diffusion model, whereas the fully asymmetric model was over-parametrized (*35*). For the axially symmetric model, the probabilities that the improvement in the fit when including additional parameters in the rotational tumbling models occurred by chance are 2.5×10^{-7}, 2.9×10^{-7}, and 1.2×10^{-5} at 300, 500, and 600 MHz, respectively. The axially symmetric rotational diffusion tensor was determined to be prolate in shape ($D_{||}/D_{\perp} > 1$) (Figure 3).

The orientation of the unique axis of the rotational diffusion tensor ($D_{||}$) with respect to the molecular structure of K122-4 pilin$^{(29-150)}$ is shown in Figure 4. The long

N-terminal α-helix of K122-4 pilin$^{(29-150)}$ has a slight kink near Gly42; thus, the helix was considered as two cylinders to calculate their orientations with respect to $D_{||}$. One helix spans residues Ala31 to Gly42 (helix I), and the other helix spans residues Leu43 to Asp54 (helix II). The long axis of helix II is oriented 33° $\pm$ 4° with respect to the orientation of $D_{||}$. Helix I and the β strands are also aligned nearly parallel to $D_{||}$ with helix I tilted 12° $\pm$ 4° to $D_{||}$. The analysis of anisotropic rotational diffusion was carried out in order to avoid misinterpretation of parameters determined when assuming isotropic rotational diffusion (see Discussion)

Model-Free Analysis and Local Motions on Different Time-Scales. Backbone amide ^{15}N relaxation parameters are widely interpreted using the Lipari−Szabo model-free approach (*30, 31*). The experimental ^{15}N-T_1, -T_2, and $\{^1H\}$-^{15}N NOE relaxation parameters were fit to spectral density models 1−5. The spectral density parameters from the 300, 500, and 600 MHz data sets were optimized separately (Figure 5), allowing consistency between the three magnetic field strengths to be assessed, as the motions giving rise to

Table 1: Rotational Diffusion Parameters by Isotropic, Axially Symmetric, and Asymmetric Models at 300, 500, and 600 MHz for K122-4 Pilin[(29−150)a]

model/ field	$\tau_m{}^b$ (ns)	$D_{\parallel}/D_{\perp}{}^c$	D_x/D_y	θ^d	ϕ^d	φ^d	E^e	$E_v{}^f$	$F_x{}^g$
isotropic [h]									
300	8.7	1	1				127.6	3.1	
500	7.6	1	1				1372.1	33.5	
600	7.3	1	1				1086.9	25.9	
ax. sym[h]									
300	8.3 ± 0.1	1.35 ± 0.02	1	83.9 ± 4.1	64.5 ± 5.2		70.9 ± 4.7	1.9 ± 0.1	10.2 ± 1.6
500	7.5	1.31 ± 0.02	1	76.7 ± 4.1	78.1 ± 6.7		534.9 ± 76.0	14.1 ± 2.0	20.5 ± 5.1
600	7.3	1.26 ± 0.02	1	83.2 ± 4.5	82.4 ± 7.0		558.2 ± 52.6	14.3 ± 1.3	12.5 ± 2.4
asym[h]									
300	8.4 ± 0.1	1.28 ± 0.19	0.90 ± 0.10	84.6 ± 5.2	64.9 ± 5.0	53.0 ± 73.0	68.9 ± 4.5	1.9 ± 0.1	0.5 ± 0.5
500	7.5	1.32 ± 0.03	0.93 ± 0.07	77.3 ± 6.5	78.9 ± 7.3	38.0 ± 54.0	505.2 ± 74.2	14.0 ± 2.1	1.1 ± 0.3
600	7.3	1.26 ± 0.02	0.96 ± 0.06	85.8 ± 5.4	81.2 ± 8.3	122.4 ± 66.0	540.0 ± 42.8	14.6 ± 1.2	0.6 ± 0.6

[a] Average and standard deviation values were calculated from the 10 best NMR structures (PDB entry 1HPW). [b] $\tau_m = 1/6D$. [c] $D_{\parallel}/D_{\perp} = 2D_z/(D_x + D_y)$. [d] Euler angles describing the orientation of the components of the diffusion tensors, D_z (θ and ϕ) and $D_{x,y}$ (φ). [e] Error function $E = \Sigma_N(T_{1,e}/T_{2,e} - T_{1,c}/T_{2,c})^2/\sigma^2_{T1/T2}$, where N is the number of residues used in the fit. [f] Reduced error function $E_v = E/(N − m)$, where N and m are the number of residues and variables used in the fit. [g] $F_x = (E_m − E_{m+x})/xE_{v,m+x}$, where E and E_v are defined above and x is the number of additional variables in the fit. Larger F_x values justify the use of the additional variables (34). [h] 42 residues at 300 and 500 MHz and 43 residues at 600 MHz from well-defined structured regions were used for the isotropic, axially symmetric, and fully asymmetric anisotropic analysis.
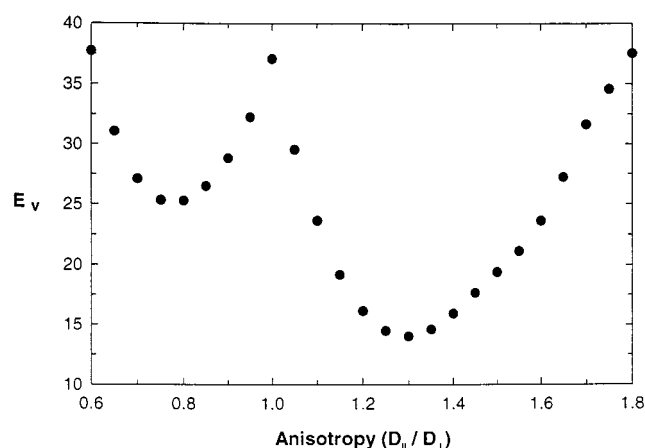

FIGURE 3: Plot of the reduced error function (E_v) with varying diffusion anisotropy for the axially symmetric model from ^{15}N relaxation data acquired at 500 MHz. E_v is as defined in Table 2. The prolate ($D_{\parallel} > D_{\perp}$) model shows a better fit than the oblate ($D_{\parallel} < D_{\perp}$) model. The overall correlation time [$(6D)^{-1} = 7.5$ ns] and the anisotropy were fixed, whereas the orientation of $D_{\parallel}$ was allowed to vary.

NMR relaxation do not depend on the magnetic field strength, apart from a very slight alignment at higher magnetic field strength (36). The S^2 values agree very well between the three magnetic field strengths (Figure 5A). In contrast, τ_e and R_{ex} values determined from 300 MHz data show large errors compared to 500 and 600 MHz data sets; thus, τ_e and R_{ex} parameters from 500 and 600 MHz data only are shown in Figure 5B,C. The larger errors in the optimized parameters from the 300 MHz data are due to significantly reduced sensitivity for NMR spectra acquired at 300 MHz compared to spectra acquired at 500 and 600 MHz. The optimized parameters τ_e, τ_s, and R_{ex} were considered physically meaningful if they exhibited appropriate temperature dependence. In addition, conformational exchange (R_{ex}) can be considered physically meaningful if a clear dependence upon magnetic field strength is observed.

The S^2 values for regions involved in secondary structure are nearly identical within error for data acquired at 300, 500, and 600 MHz (Figure 5A). The average S^2 values at 500 MHz for regions of secondary structure are 0.91, 0.86,
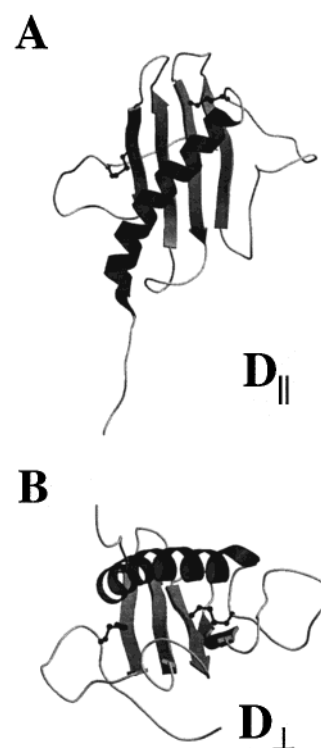

FIGURE 4: Structure of K122-4 pilin[(29−150)] oriented with respect to the unique axis of the axially symmetric rotational diffusion tensor ($D_{\parallel}$). (A) $D_{\parallel}$ lies in the plane of the page. The β-strands and the N-terminal half of the α-helix are nearly parallel to $D_{\parallel}$, whereas the C-terminal half of the α-helix is tilted ~33° to the direction of $D_{\parallel}$ (see text). (B) Structure rotated by 90° about the x-axis ($D_{\perp}$). The figure was created using the program MolScript v2.1.1 (57).

0.87, 0.89, and 0.85 for the α-helix and βI-, βII-, βIII-, and βIV-strands, respectively. These S^2 values are typical of well-defined secondary structure in proteins. Pilin is believed to self-associate via N-terminal helical residues in order to form type-IV pilus fibers (1). In this study, the partly truncated N-terminal α-helix maintains S^2 values typical of well-defined secondary structure throughout its length. The N- and C-termini and loop regions between elements of secondary structure exhibit motions of varying amplitudes and rates. Apart from the N- and C-terminal random coil regions,
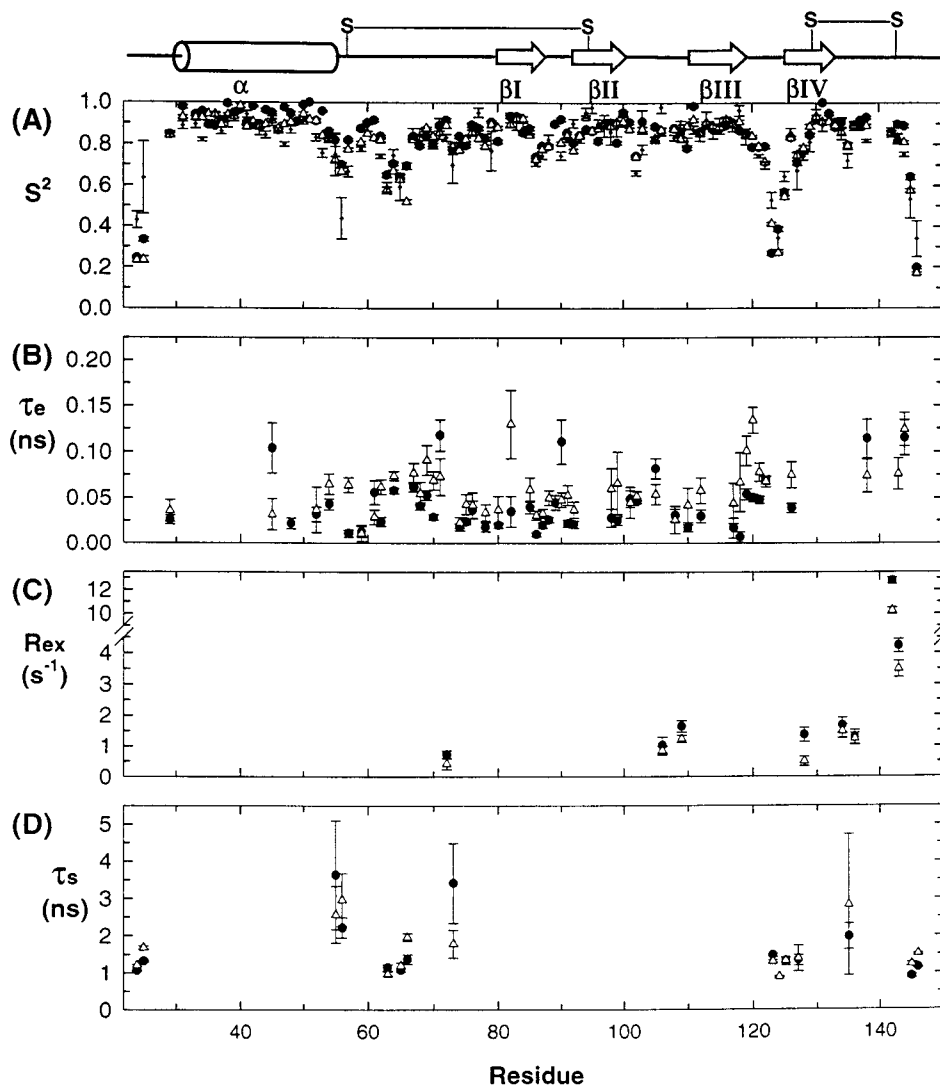
FIGURE 5: Plots of (A) order parameters (S^2), (B) correlation times for internal motions (τ_e) from the $S^2-\tau_e$ model, (C) conformational exchange terms (R_{ex}), and (D) correlation times for slow internal motions (τs) faster than τ_m but slower than τ_e, from 300 (+), 500 ($\triangle$), and 600 MHz data ($\bullet$). 300 MHz data are plotted in panel (A) only.

decreased S^2 values ($S^2 < 0.85$) are observed for the loop between the α-helix and strand βI (residues Ala63-Thr64-Ala65-Gly66), and residues Gly123-Ser124-Tyr125 for the loop between strands βIII and βIV.

Internal motions within the $10^{-10}-10^{-12}$ s time-scale ($0 < \tau_e < \tau_m$) are found throughout the loop regions between elements of regular secondary structure (Figure 5B). The C-terminal region of the α-helix and the first residue of strand βI also show increased internal motions on the subnanosecond to picosecond time-scale, as evidenced by lower S^2 and larger τ_e values compared to other regions of well-defined secondary structure. For most residues, τ_e values are less than 100 ps (Figure 5B). Nanosecond time-scale internal motions faster than τ_m but slower than τ_e are observed for loops connecting the α-helix and βI-strand, and the βIII- and βIV-strands, Asn135 within the first β-turn of the C-terminal disulfide loop, and also the N-terminal and C-terminal random coil regions (Figure 5D). The τ_s values for these motions range from 1 to 4 ns. Associated with these slow internal motions in loop or coil regions are reduced slow time-scale order parameters (S_s^2), implying increased amplitude conformational fluctuations with time constant τ_s.

Motion occurring on the micro- to millisecond time-scale can contribute to a decrease in the expected ^{15}N-T_2 values. T_2 values for Cys142 and Gln143 exhibit a pronounced decrease (Figure 2B), indicating potential conformational exchange phenomena for these residues. The inclusion of an R_{ex} term in the theoretical expression for T_2 with the model-free analysis for residues Asp72, Thr106, Arg109, Ala128, Asp134, Lys136, Cys142, and Gln143 (Figure 5C) led to improvement in the agreement between calculated and experimental T_2 values. The calculated R_{ex} values for these residues show a consistent decrease with increasing temperature, indicating the presence of genuine slow conformational exchange phenomena contributing to decreases in expected T_2 values (Table 2). In particular, Cys142 in the disulfide loop shows a R_{ex} term 10-fold larger than that for other residues at 15 °C and 500 MHz (Table 2). However, the disulfide bond partner (Cys129) that forms part of strand βIV does not require a R_{ex} term in order to account properly for the experimentally determined T_2. The R_{ex} terms for residues Asp72, Thr106, Arg109, Ala128, Asp134, Lys136, Cys142, and Gln143 also display a dependence on magnetic field strength (Table 2), though the magnitude tends to be

Table 2: Conformational Exchange of K122-4 Pilin$^{(29-150)}$ from Backbone Amide ^{15}N Relaxation Parameters at Various Temperatures and Magnetic Field Strengths

	R_{ex} (s^{-1})						
	temperature (°C)[a]				magnetic field (MHz)[b]		
residue	5	15	25	35	30.394	50.653	60.795
Asp72	6.28 ± 1.64	3.26 ± 0.32	1.13 ± 0.26	nd[c]	nf[d]	0.42 ± 0.18	0.72 ± 0.13
Thr106	4.22 ± 1.10	2.41 ± 0.40	1.30 ± 0.22	0.93 ± 0.44	nf[d]	0.84 ± 0.14	1.02 ± 0.27
Arg109	5.21 ± 1.13	2.35 ± 0.34	2.01 ± 0.26	1.24 ± 0.42	1.35 ± 0.44	1.23 ± 0.12	1.64 ± 0.19
Ala128	2.18 ± 0.50	nf[d]	0.74 ± 0.17	0.32 ± 0.62	0.24 ± 0.42	0.50 ± 0.16	1.36 ± 0.23
Asp134	4.92 ± 1.52	2.85 ± 0.43	3.37 ± 0.43	0.94 ± 0.46	2.46 ± 0.99	1.45 ± 0.22	1.67 ± 0.26
Lys136	8.31 ± 2.17	3.64 ± 0.57	2.86 ± 0.31	0.69 ± 0.40	0.42 ± 0.39	1.23 ± 0.20	1.28 ± 0.23
Cys142	nf[d]	30.8 ± 1.67	14.4 ± 0.44	8.36 ± 0.55	4.91 ± 0.98	10.2 ± 0.28	12.8 ± 0.27
Gln143	3.73 ± 2.17	4.89 ± 0.45	4.48 ± 0.32	2.64 ± 0.39	3.01 ± 0.76	3.48 ± 0.26	4.23 ± 0.22

[a] Relaxation parameters were obtained at 500 MHz. [b] Relaxation parameters were obtained at 30 °C. Field strength is given as the ^{15}N Larmor frequency in MHz. [c] Not determined due to spectral overlap. [d] Not fitted due to large errors.

smaller than expected. These results are consistent with conformational exchange phenomena contributing to decreased T_2 relaxation times for these residues.

Inclusion of R_{ex} terms improved the fit for the relaxation data of residues within the α-helix in the model-free analysis. Failure to take rotational diffusion anisotropy into account can lead to the misidentification of R_{ex} terms as genuine conformational exchange (33, 34). Calculation of T_2 values using spectral density functions appropriate for axially symmetric rotational diffusion anisotropy (see Table 1) is sufficient to account for the experimental T_2 values in the N-terminal α-helix. In addition, the inconsistent field and temperature dependence of R_{ex} terms for the α-helix are indicative that conformational exchange is not genuine. It should be noted that S^2 values for the α-helix remain essentially the same whether isotropic or anisotropic rotational diffusion is employed in the spectral density function. As shown in Figure 4, the α-helix is slightly tilted with respect to the orientation of $D_{||}$, whereas the β-strands are nearly parallel to $D_{||}$. N–NH bond vectors are oriented nearly parallel to the helical axis in an α-helix, but perpendicular to the direction of the strand within β-strands. Hence, the N–NH bond vectors within the α-helix of pilin$^{(29-150)}$ are nearly parallel with the unique axis of the diffusion tensor, while those in the β-strands are perpendicular to $D_{||}$. The unique orientation of the α-helix of pilin$^{(29-150)}$ with respect to $D_{||}$ accounts for the conformational exchange terms observed in the α-helix when analyzed with the model-free approach, assuming isotropic rotational diffusion.

DISCUSSION

Full-length *P. aeruginosa* pilin is known to oligomerize in solution due to its long, hydrophobic α-helix (37, 38). Recently, partial truncation of this hydrophobic α-helix was reported to prevent oligomerization without loss of biological activity. N-terminally truncated forms of pilin have been employed to determine the crystal structure of PAK pilin (12) and the solution structure of *P. aeruginosa* K122-4 pilin$^{(29-150)}$ (Keizer et al., unpublished). The calculated molecular mass of unlabeled K122-4 pilin$^{(29-150)}$ is 11 305 Da, and the overall molecular correlation time for monomeric pilin$^{(29-150)}$ is expected to be ∼6.7 ns (39). The experimental τ_m obtained from backbone amide ^{15}N relaxation parameters (Table 1) indicates that K122-4 pilin$^{(29-150)}$ exists largely as a monomer under the solution conditions used in this study. This result is in good agreement with results from sedimen-

tation equilibrium experiments and mass spectrometry that indicate that the molecular mass of pilin$^{(29-150)}$ is ∼13 100 Da, and is monomeric at the concentration employed in this study (Keizer et al., unpublished).

The precision of a structure determined from NMR data can be appreciated in terms of backbone rmsd and angular order parameters (40, 41). Low backbone rmsd values and angular order parameters of ∼1 for backbone ϕ and ψ dihedral angles, $S(\phi)$ and $S(\psi)$, respectively, indicate high precision for regions of secondary structure, whereas large rmsd and lower values of $S(\phi)$ and $S(\psi)$ indicate disordered regions, typically found in linker loops and terminal regions (Figure 6). Interestingly, backbone amide N–NH S^2 values do not display good correlation with backbone rmsd and $S(\phi)$ and $S(\psi)$ values. That is, regions of disorder in the solution structures are not necessarily flexible, and well-defined regions are not necessarily rigid on the time-scale accessible to backbone amide ^{15}N relaxation measurements. For example, the loop between strands βIII and βIV (Gly123-Ser124-Tyr125) exhibits large-amplitude internal motions for the backbone N–NH bond vectors (low S^2). However, only small deviations from rmsd and $S(\phi)$ and $S(\psi)$ values expected for well-defined regions of secondary structure are observed for a part of the loop (Asp121-Lys122-Gly123). In addition, the loop between strands βII and βIII is not well-defined in the solution structures, but displays S^2 values typical of well-defined secondary structure. It is also noteworthy that micro- to millisecond time-scale motions for the β-turns in the disulfide loop are not evident from rmsd and $S(\phi)$ and $S(\psi)$ values. The discrepancy between disorder in the solution structures and backbone flexibility determined from ^{15}N relaxation measurements may be explained in part by assuming that a number of different sub-states are available for flexible residues, and one sub-state possesses a strong NOE contact between protons. This NOE could dominate the sub-state represented within the ensemble of NMR structures. On the other hand, a lack of NOE restraints due to spectral overlap, chemical shift ambiguity, or experimental errors will result in lower precision for structured regions that appear rigid from backbone amide ^{15}N relaxation measurements.

Residues with increased flexibility are found within the loop regions of K122-4 pilin$^{(29-150)}$ (residues 63–66 and 123–125) (Figure 5A). Based on predictions from an analysis of residue hydrophobicity for PAK pilin, several surface regions, including regions within the loops, were
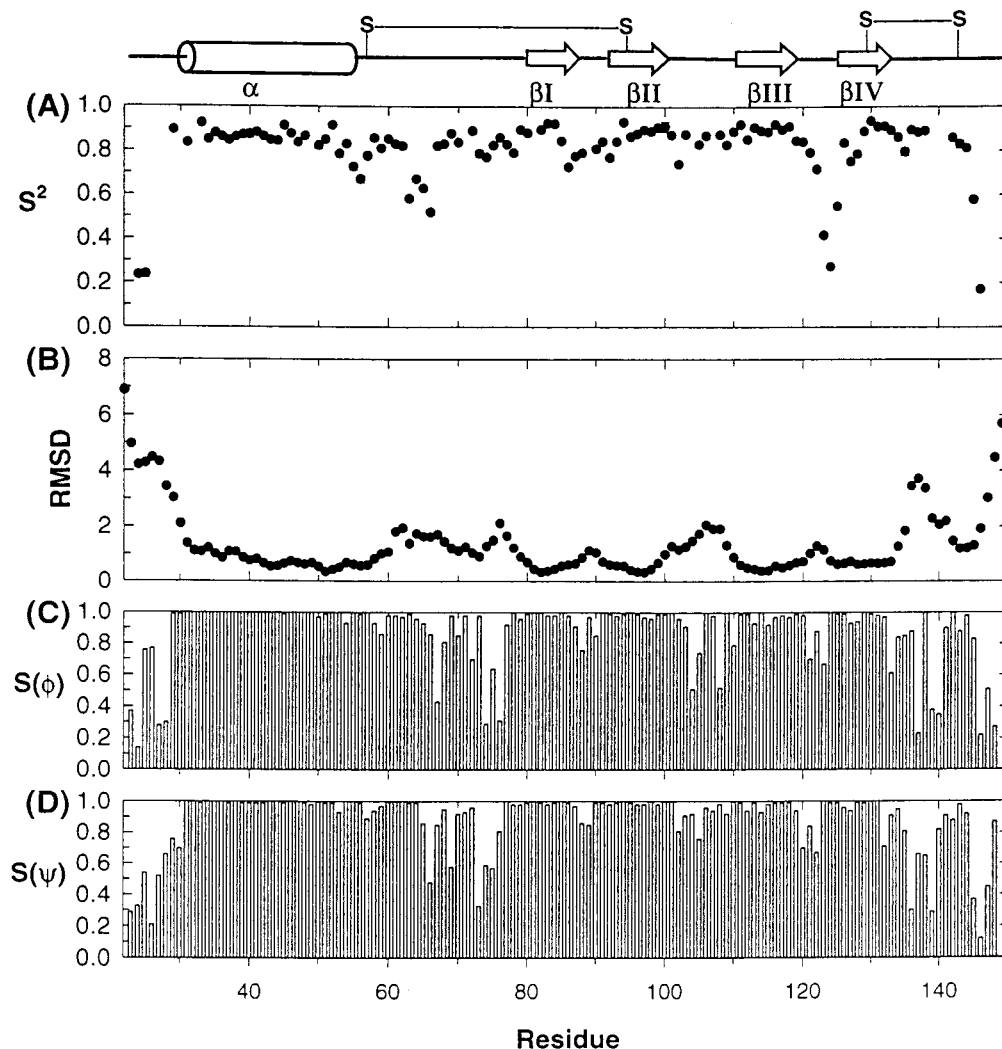
FIGURE 6: Comparison of (A) order parameters (S^2) for backbone amide ^{15}N nuclei at 500 MHz, (B) backbone rmsd for the ensemble of NMR structures, and backbone angular order parameters for (C) ϕ and (D) ψ dihedral angles. The rmsd and angular order parameters were calculated from the ensemble of 10 NMR structures.

found to induce antisera that react with pili using direct ELISA (*42*). As K122-4 pilin is also likely to display antigenic surface regions with different antigenicities, it would be of interest to examine the correlation between loop mobility and antigenicity in future studies.

Structural studies using pilin peptides have revealed a conserved disulfide-bridged, two β-turn motif in the C-terminal receptor binding domain (*16, 17*), corresponding to residues Asp134-Asn135-Lys136-Tyr137 for one β-turn, and Pro139-Lys140-Thr141-Cys142 for the other β-turn in K122-4 pilin$^{(29-150)}$. In the protein, five residues at the N-terminus of the disulfide loop (Cys129-Thr130-Ser131-Asn132-Ala133) contribute to strand βIV. For K122-4 pilin$^{(29-150)}$, residues in the disulfide loop exhibit S^2 values expected for structured residues, while residues in the β-turns manifest conformational exchange, that is, potentially genuine micro- to millisecond time-scale motion, particularly residues Asp134, Lys136, and Cys142. Additionally, slow nanosecond time-scale internal motions ($\tau_e < \tau_s < \tau_m$) are observed for Asn135. Unfortunately, Lys140 and Thr141 could not be unambiguously assigned in the spectra and thus could not be included in the dynamics analysis. Hence, the C-terminal disulfide loop is rigid with respect to fast picosecond time-scale motions, but displays slow micro- to

millisecond time-scale motions within the β-turns of the disulfide loop particularly for residues Asp134-Lys136 and Cys142. The pronounced conformational exchange for Cys142 may be the result of isomerization of the disulfide bond between the side chains of Cys129 and Cys142. Conformational exchange contributions to backbone amide ^{15}N-T_2 relaxation times resulting from isomerization of disulfide bonds have been reported for basic pancreatic trypsin inhibitor (*43*) and fibronectin (*44*). This isomerization involves exchange between two conformations with different chirality for the disulfide bond. Thus, the decreased ^{15}N-T_2 relaxation times for Cys142 as well as those for Gln143 can potentially be explained by disulfide bond isomerization. Interestingly, Cys129, the disulfide-bonded partner for Cys142, does not show appreciably decreased ^{15}N-T_2 relaxation times, likely as a result of involvement in secondary structure within strand βIV.

Peptide studies of the C-terminal disulfide loop in pilin have indicated that it assumes a role in receptor binding and in interacting with antibodies (*42, 45*). The conformational restriction of the C-terminal loop by the disulfide bridge appears to be critical for binding of peptides from this region to host cell surface receptors, as oxidized peptides bind to A549 human lung carcinoma cells, whereas reduced peptides

do not (*46*). As the disulfide loop does not exhibit flexibility for backbone dynamics on the fast picosecond time-scale, we suggest that a rigid main chain conformation is important for proper attachment of bacterial pili to host cell surface receptors. Despite diverse sequence variations for the C-terminal disulfide loop, pilin proteins from different *P. aeruginosa* strains have been shown to recognize the same receptor analogues (*47*), and share a common β-turn motif in their disulfide loops (*48*). To maintain a favorable recognition interface for the receptor, it is likely that the disulfide loop utilizes a rigid backbone conformation, at least on the fast picosecond time-scale, as a scaffold for binding to the host cell receptor. This assumption is supported by previous results indicating that the backbone conformation of the disulfide loop region does not undergo significant changes upon binding to a receptor analogue (*49*).

A rigid backbone appears important for receptor binding; however, slow motions (μs−ms) also play a role in mediating the interactions of the C-terminal disulfide loop. Asp134, Lys136, and Cys142 residues that are located within β-turns in the C-terminal disulfide loop region and important for receptor binding show micro- to millisecond time-scale conformational fluctuations. Slow time-scale (μs−ms) motions for the β-turns of the C-terminal disulfide loop have been previously observed for peptides comprising this domain of PAK pilin (*50*). Additionally, a disulfide-bridged peptide from nerve growth factor shows conformational exchange within a β-turn, similar to the C-terminal disulfide loop in K122-4 pilin$^{(29−150)}$ (*51*). Interestingly, the β-turn motif in the nerve growth factor peptide interacts with cell surface neurotrophin receptor TrkA. These results draw attention to the relationship between multiplicity in protein conformation and receptor recognition. The exact role of conformational exchange within the C-terminal disulfide loop in receptor binding is not yet clear. Slow time-scale motions of the loop within the vicinity of Cys142 and Asp134−Lys136 are likely to alter the orientation of the β-turns with respect to the pilin protein, and this may allow pilin proteins from different strains to obtain a reasonable conformation for receptor binding.

It has been reported that a β-turn motif can serve as a common antibody recognition motif (*52, 53*). The β-turn motif within the C-terminal disulfide loop in pilin has been shown to be antigenic (*15, 48*). The role of the disulfide bond in determining antigenicity is less clear, because a seven residue linear peptide lacking the disulfide bridge forms the epitope of the monoclonal antibody PK99H for PAK pilin (*54*). However, as the residues in the epitope are located in β-turns as determined from structural studies of peptides and the intact pilin protein, it is likely that the conformation of the epitope involved in antibody recognition is the β-turn motif. The cross-reactivity of PAK-13 antibody to different *P. aeruginosa* strains suggests that they share a common structural motif for antigenicity (*49, 55*). The rigid backbone conformation with respect to fast picosecond time-scale motions for the antigenic region is likely to contribute in part to the cross-reactivity across *P. aeruginosa* strains. With limited flexibility at the recognition site, the hydrophobic or electrostatic properties of the side chain in situ should be important factors for interactions with antibodies. This is reflected in a study that involves antibody PAK-13, in which *P. aeruginosa* strain CD4 showed the best binding to the antibody (*54*). Our results support the "induced fit" mechanism in which the conformation for the antibody interaction surface is induced by the structure of the antigenic determinant (*56*). An understanding of the molecular determinants for antibody recognition should give insight into cross-reactivity in immune responses, and aid in the design of more efficient vaccines against a variety of pathogenic bacteria.

SUPPORTING INFORMATION AVAILABLE

Supporting Information available includes T_1, T_2, NOE, and order parameters at each of the field strengths used in this study (7 pages). This material is available free of charge via the Internet at http://pubs.acs.org.

REFERENCES

1. Forest, K. T., and Tainer, J. A. (1997) *Gene 192*, 165−169.
2. Farinha, M. A., Conway, B. D., Glasier, L. M., Ellert, N. W., Irvin, R. T., Sherburne, R., and Paranchych, W. (1994) *Infect. Immun. 62*, 4118−4123.
3. Karaolis, D. K., Somara, S., Maneval, D. R., Jr., Johnson, J. A., and Kaper, J. B. (1999) *Nature 399*, 375−379.
4. Doig, P., Todd, T., Sastry, P. A., Lee, K. K., Hodges, R. S., Paranchych, W., and Irvin, R. T. (1988) *Infect. Immun. 56*, 1641−1646.
5. Roncero, C., Dareins, A., and Casadaban, M. J. (1990) *J. Bacteriol. 172*, 1899−1904.
6. Whitchurch, C. B., and Mattick., J. S. (1994) *Mol. Microbiol. 13*, 1079−1091.
7. Wall, D., and Kaiser, D. (1999) *Mol. Microbiol. 32*, 1−10.
8. Merz, A. J., So, M., and Sheetz, M. P. (2000) *Nature 407*, 98−102.
9. Dalrymple, B., and Mattick, J. S. (1987) *J. Mol. Evol. 25*, 261−269.
10. Mattick, J. S., Whitchurch, C. B., and Alm, R. A. (1996) *Gene 179*, 147−155.
11. Parge, H. E., Forest, K. T., Hickey, M. J., Christensen, D. A., Getzoff, E. D., and Tainer, J. A. (1995) *Nature 378*, 32−38.
12. Hazes, B., Sastry, P. A., Hayakawa, K., Read, R. J., and Irvin, R. T. (2000) *J. Mol. Biol. 299*, 1005−1017.
13. Marceau, M., and Nassif, X. (1999) *J. Bacteriol. 181*, 656−661.
14. Lee, K. K., Doig, P., Irvin, R. T., Paranchych, W., and Hodges, R. S. (1994) *Mol. Microbiol. 11*, 705−713.
15. Doig, P., Sastry, P. A., Hodges, R. S., Lee, K. K., Paranchych, W., and Irvin, R. T. (1990) *Infect. Immun. 58*, 124−130.
16. McInnes, C., Sönnichsen, F. D., Kay, C. M., Hodges, R. S., and Sykes, B. D. (1993) *Biochemistry 32*, 13432−13440.
17. Campbell, A. P., Bautista, D. L., Tripet, B., Wong, W. Y., Irvin, R. T., Hodges, R. S., and Sykes, B. D. (1997) *Biochemistry 36*, 12791−12801.
18. Kay, L. E. (1998) *Nat. Struct. Biol. NMR Suppl.*, 513−517.
19. Stock, A. (1999) *Nature 400*, 221−222.
20. Ishima, R., and Torchia, D. A. (2000) *Nat. Struct. Biol. 7*, 740−743.
21. Kay, L. E., Muhandiram, D. R., Wolf, G., Shoelson, S. E., and Forman-Kay, J. D. (1998) *Nat. Struct. Biol. 5*, 156−163.
22. Yang, D., and Kay, L. E. (1996) *J. Mol. Biol. 263*, 369−382.

23. Yang, D., Mok, Y. K., Forman-Kay, J. D., Farrow, N. A., and Kay, L. E. (1997) *J. Mol. Biol. 272*, 790−804.

24. Farrow, N. A., Muhandiram, R., Singer, A. U., Pascal, S. M., Kay, C. M., Gish, G., Shoelson, S. E., Pawson, T., Forman-Kay, J. D., and Kay, L. E. (1994) *Biochemistry 33*, 5984−6003.

25. Spyracopoulos, L., Gagné, S. M., Li, M. X., and Sykes, B. D. (1998) *Biochemistry 37*, 18032−18044.

26. Delaglio, F., Grzesiek, S., Vuister, G. W., Zhu, G., Pfeifer, J., and Bax, A. (1995) *J. Biomol. NMR 6*, 277−293.

27. Keizer, D. W., Kalisiak, M., Crump, M. P., Suh, J. Y., Irvin, R. T., and Sykes, B. D. (2001) *J. Biomol. NMR* (in press).

28. Johnson, B. A., and Blevins, R. A. (1994) *J. Biomol. NMR 4*, 603−614.

29. Abragam, A. (1961) *Principles of Nuclear Magnetism*, Clarendon Press, Oxford, U.K.

30. Lipari, G., and Szabo, A. (1982) *J. Am. Chem. Soc. 104*, 4546−4559.

31. Lipari, G., and Szabo, A. (1982) *J. Am. Chem. Soc. 104*, 4559−4570.

32. Barbato, G., Ikura, M., Kay, L. E., Pastor, R. W., and Bax, A. (1992) *Biochemistry 31*, 5269−5278.

33. Tjandra, N., Wingfield, P., Stahl, S., and Bax, A. (1995) *J. Am. Chem. Soc. 117*, 12562−12566.

34. Gagné, S. M., Tsuda, S., Spyracopoulos, L., Kay, L. E., and Sykes, B. D. (1998) *J. Mol. Biol. 278*, 667−686.

35. Bevington, P. R., and Robinson, D. K. (1992) *Data Reduction and Error Analysis for the Physical Science*, 2nd ed., McGraw-Hill, New York.

36. Tjandra, N., Grzesiek, S., and Bax, A. (1996) *J. Am. Chem. Soc. 118*, 6264−6272.

37. Watts, T. H., Scrabba, D. G., and Paranchych, W. (1982) *J. Bacteriol. 151*, 1508−1513.

38. Watts, T. H., Kay, C. M., and Paranchych, W. (1983) *Biochemistry 22*, 3640−3646.

39. Spyracopoulos, L., Gagné, S. M., and Sykes, B. D. (2000) *Proceedings for the International School of Structural Biology and Magnetic Resonance 4th Course on Protein Dynamics, Function and Design*, Plenum Press, New York (in press).

40. Pallaghy, P. K., Duggan, B. M., Pennington, M. W., and Norton, R. S. (1993) *J. Mol. Biol. 234*, 405−420.

41. Hyberts, S. G., Goldberg, M. S., Havel, T. F., and Wagner, G. (1992) *Protein Sci. 1*, 736−751.

42. Lee, K. K., Doig, P., Irvin, R. T., Paranchych, W., and Hodges, R. S. (1989) *Mol. Microbiol. 3*, 1493−1499.

43. Szyperski, T., Luginbühl, P., Otting, G., Güntert, P., and Wüthrich, K. (1993) *J. Biomol. NMR 3*, 151−164.

44. Phan, I. Q. H., Boyd, J., and Campbell, I. D. (1996) *J. Biomol. NMR 8*, 369−378.

45. Paranchych, W., Sastry, P. A., Volpel, K., Loh, B. A., and Speert, D. P. (1986) *Clin. Invest. Med. 9*, 113−118.

46. Wong, W. Y., Campbell, A. P., McInnes, C., Sykes, B. D., Paranchych, W., Irvin, R. T., and Hodges, R. S. (1995) *Biochemistry 34*, 12963−12972.

47. Sheth, H. B., Lee, K. K., Wong, W. Y., Srivastava, G., Hindsgaul, O., Hodges, R. S., Paranchych, W., and Irvin, R. T. (1994) *Mol. Microbiol. 11*, 715−723.

48. Campbell, A. P., McInnes, C., Hodges, R. S., and Sykes, B. D. (1995) *Biochemistry 34*, 16255−16268.

49. Campbell, A. P., Wong, W. Y., Houston, M., Jr., Schweizer, F., Cachia, P. J., Irvin, R. T., Hindsgaul, O., Hodges, R. S., and Sykes, B. D. (1997) *J. Mol. Biol. 267*, 382−402.

50. Campbell, A. P., Spyracopoulos, L., Irvin, R. T., and Sykes, B. D. (2000) *J. Biomol. NMR 17*, 239−255.

51. Beglova, N., LeSauteur, L., Ekiel, I., Saragovi, U., and Gehring, K. (1998) *J. Biol. Chem. 273*, 23652−23658.

52. Stanfield, R. L., Fieser, T. M., Lerner, R. A., and Wilson, I. A. (1990) *Science 248*, 712−719.

53. Garcia, K. C., Ronco, P. M., Verroust, P. J., Brunger, A. T., and Amzel, L. M. (1992) *Science 257*, 502−507.

54. Wong, W. Y., Irvin, R. T., Paranchych, W., and Hodges, R. S. (1992) *Protein Sci. 1*, 1308−1318.

55. Sheth, H. B., Glasier, L. M. G., Ellert, N. W., Cachia, P., Kohn, W., Lee, K. K., Paranchych, W., Hodges, R. S., and Irvin, R. T. (1995) *Biomed. Pept., Proteins Nucleic Acids 1*, 141−148.

56. Rini, J. M., Schulze-Gahmen, U., and Wilson, I. A. (1992) *Science 255*, 959−965.

57. Kraulis, P. J. (1991) *J. Appl. Crystallogr. 24*, 946−950.

BI002524H